

A dynamic-relaxation formulation for analysis of cable structures with sliding-induced friction

Nizar Bel Hadj Ali^a, Ann C. Sychterz^b and Ian F.C. Smith^b

^aLASMAP, Ecole Polytechnique de Tunisie, University of Carthage, B.P. 743, La Marsa 2078, Tunisia

^bApplied Computing and Mechanics Laboratory (IMAC), School of Architecture, Civil, and Environmental Engineering (ENAC), École Polytechnique Fédérale de Lausanne (EPFL), 1015 Lausanne, Switzerland

Structure of the paper

Abstract

1. Introduction
 2. Governing equations of a sliding cable accounting for frictional effects
 3. The proposed DR implementation
 - 3.1 Governing equations
 - 3.2 Fictitious mass calculation
 - 3.3 Residual forces
 4. Numerical examples
 - 4.1 A continuous cable sliding through fixed nodes
 - 4.2 A tensegrity-based beam
 - 4.3 Deployment of a tensegrity footbridge
 5. Conclusions
-

Abstract

In many cable structures, special types of joints are designed to allow cables to slide freely along the joints. Thus, a number of discrete cable elements are substituted by a single continuous cable that slides over multiple nodes. Continuous cables are employed in engineering applications such as cranes, domes, tensioned membranes and tensegrity structures. Most studies involve the assumption of frictionless movement of cable elements through pulleys. Nevertheless, frictionless sliding is usually an unrealistic hypothesis. In this paper, the dynamic relaxation (DR) method is extended to accommodate friction effects in tensioned structures that include continuous cables. The applicability of this DR formulation is demonstrated through analysis of three case studies that involve both numerical and experimental investigation. Results show potential to efficiently accommodate sliding-induced friction.

Keywords: sliding cables, friction effects, cable structures, dynamic relaxation.

1. Introduction

Cables that run continuously through nodes are employed in engineering applications such as domes, cranes, tensioned membranes and tensegrity structures. It is becoming a common practice to group individual cable elements into continuous cables. A single continuous cable moves over multiple nodes through pulleys and sliding contact joints. In cable structures, the tensioning process includes adjustment of cable length in order to establish the required stress state. Such situations demonstrate one of the most important advantages of using continuous cables. Rather than controlling multiple cable elements, connecting cables allows simultaneous control of cable groups using only one control device [1]. This is also the case for active and deployable structures that are controlled by cable length adjustment [2-5].

With regards to structural behavior, using continuous cables may significantly change the structural response of cable structures. A cable sliding over multiple nodes causes changes in the internal force distribution and increases flexibility. This consequently affects static and dynamic behavior. In addition, in actively-controlled structures, using continuous cables inevitably reduces structure controllability since an active continuous cable cannot effectively control all the nodes it passes through.

Finite element (FE) formulations for continuous cable elements were developed for modeling of suspension systems [6-9] and fabric structures [10]. Aufaure [6] pioneered the analysis of continuous cables and developed a finite element of cable passing through a pulley. The finite element allowed the cable hanging process to be modeled for multispans electric transmission lines. Pauletti [11] extended Aufaure's formulation and presented a geometrically exact formulation of a cable finite element allowing sliding with friction. Kwan and Pellegrino [12] proposed a matrix formulation for an active-cable macro-element consisting of two or more straight segments. The authors derived the equilibrium and flexibility matrices of active cable elements and pantographic elements used in deployable structures. Zhou et al [13] developed a sliding-cable-element to simulate parachute folding. Chen et al [14] presented a formulation of sliding-cable-element with multiple nodes for the analysis of Suspen-Dome structures.

Lee et al [15] derived the tangent stiffness matrix of a continuous cable including frictional effects. The geometric stiffness of the proposed cable element was not taken into account in the formulation limiting thus its applicability to linear elastic behaving structures [16]. In the tensegrity-concept research framework, Genovese [17] investigated an approach to form-finding and analysis of tensegrity structures with sliding cables (clustered tensegrities). Moored and Bart-Smith [18] formulated the potential energy, equilibrium equations and stiffness matrix for tensegrity structures with continuous cables. They proposed the term “*clustered tensegrity*” to denote the particular class of tensegrity structures having continuous cables. Recently, Zhang et al [19, 20] employed a co-rotational formulation to derive a finite element formulation for nonlinear analysis of clustered tensegrities.

Compared with the direct stiffness-analysis approach, the dynamic relaxation method (DR) is a more time-efficient alternative for the analysis of structural systems with material and geometrical nonlinearities. This method, introduced by Otter [21] and Day [22] in the mid-1960s, is based on an explicit iterative method for the static solution of structural-mechanics problems [7]. When the DR method is used, the static case is transformed into a pseudo-dynamic case by introducing fictitious inertia and damping terms in the equation of motion. The DR method traces the motion of each node of a structure until the structure comes to rest in static equilibrium. DR has been used to solve a wide variety of engineering problems [23-29]. Particularly attractive for tension structures [30, 31], the DR method has been applied to analysis of cable structures with continuous cables. Bel Hadj Ali et al [32] has proposed modifications to the DR method for clustered tensegrity structures. Hincz [9] and Pauletti et al [8, 33] have also investigated DR for nonlinear analysis of arch-supported cable-net structures and membrane structures, respectively.

Most studies of clustered cables involve assumptions of frictionless movement of cable elements through pulleys. However, frictionless movement is an unrealistic hypothesis. This has been shown experimentally [34-37].

Liu et al [34] experimentally studied pre-stressing of “suspension-dome” structures. Experimental tests performed on a 10.8m span scaled-dome-prototype revealed that the friction coefficient at sliding nodes varies between 0.1 and 0.5 depending on material properties and stress level in

cable elements. Results also showed that axial force deviations from values determined assuming no friction exceeded 30% for some cables. Recent studies related to sliding cables by Veuve et al. [35, 36] involved deployment of a tensegrity footbridge that was studied numerically and experimentally. Additional investigation by Sychterz and Smith [37] showed that the structural behavior cannot be modelled satisfactorily using the assumption of friction-free cables sliding across joints.

In this paper, the DR method is adapted for the analysis of cable structures with sliding-induced friction. Section 2 contains a presentation of the governing equations of a sliding cable accounting for frictional effects. The subsequent section introduces the proposed analysis formulation based on the dynamic relaxation method. Basic DR steps, determination of residual forces and masses as well as the damping strategy are described. Case studies are presented in Section 4. In the first case study, the new algorithm is validated by simulating a continuous cable sliding through multiple nodes. Results are compared with those obtained employing existing FE-based methodologies to show the effectiveness of the DR formulation. In the second case study, load response and actuation of an active tensegrity beam are investigated. The third case study is concerned with the deployment analysis of a tensegrity-based footbridge. Numerical and experimental results are compared and discussed.

2. Governing equations of a sliding cable accounting for frictional effects

Consider the two-element structure shown in Fig. 1(a). The unconstrained reference node 2 is connected to nodes 1 and node 3 by one sliding/clustered cable composed of two sub-elements, e_1 and e_2 . The sliding cable runs over a small pulley at node 2.

The characteristics of the continuous cable can be easily written in terms of the characteristics of the two cable sub-elements. The continuous cable length, l , is the sum of sub-elements element lengths (Eq.1), where subscript 1 and 2 denote sub-elements numbers.

$$l = l_1 + l_2 \quad (1)$$

Equivalently, the non-loaded length, l_0 , of the continuous cable may be defined in the same way (Eq.2).

$$l_0 = l_{0,1} + l_{0,2} \quad (2)$$

With the assumption that the cable slides over node 2 with no friction, the continuous cable can be assumed as a string of cable sub-elements all carrying the same tensile force t . The axial force in the continuous cable is thus given by Eq.3 where E is Young's modulus of elasticity and A is the cross section area of the cable.

$$t_1 = t_2 = t = EA \frac{l - l_0}{l_0} \quad (3)$$

The sliding length at node 2, denoted s_2 (Fig. 1(a)), represents the length of cable portion that was exchanged between the two sub-elements. Assuming frictionless sliding, the sliding length s_2 is not explicitly taken into account in the governing equation of the continuous cable (Eq.3).

The nodes of the clustered cable have position vectors, \mathbf{x}_1 , \mathbf{x}_2 and \mathbf{x}_3 , relative to some reference. Unit vectors, \mathbf{c}_1 and \mathbf{c}_2 define the direction of each of the two cable sub-elements (Eq.4).

$$\mathbf{c}_1 = (\mathbf{x}_2 - \mathbf{x}_1) / l_1 \quad ; \quad \mathbf{c}_2 = (\mathbf{x}_3 - \mathbf{x}_2) / l_2 \quad (4)$$

For cable sub-element e_1 , nodal force vectors \mathbf{F}_1 and \mathbf{F}_{21} , illustrated in Fig. 1(b), are in equilibrium with internal tension in the cable (Eq.5).

$$\begin{aligned} \mathbf{F}_1 &= -\mathbf{c}_1 t \\ \mathbf{F}_{21} &= \mathbf{c}_1 t \end{aligned} \quad (5)$$

Equivalently, for sub-element e_2 , nodal forces \mathbf{F}_{22} and \mathbf{F}_3 are related to the internal tension in the cable through Eq.6.

$$\begin{aligned} \mathbf{F}_{22} &= -\mathbf{c}_2 t \\ \mathbf{F}_3 &= \mathbf{c}_2 t \end{aligned} \quad (6)$$

Equilibrium equations of the structure can be written in terms of a unique axial internal force, t , in the cable. Combining Eq. 5 and Eq.6, equilibrium equations at nodes 1, 2 and 3 are presented in Eq.7.

$$\begin{aligned}
\mathbf{F}_1 &= -\mathbf{c}_1 t \\
\mathbf{F}_2 &= \mathbf{F}_{21} + \mathbf{F}_{22} = (\mathbf{c}_1 - \mathbf{c}_2)t \\
\mathbf{F}_3 &= \mathbf{c}_2 t
\end{aligned} \tag{7}$$

Based on the governing equations expressed in Eq.7, a continuous cable can be easily incorporated into structural analysis such as DR [32]. The component equilibrium expressions could also be differentiated with respect to node coordinates in order to find the tangent stiffness matrix of the sliding cable [18, 19].

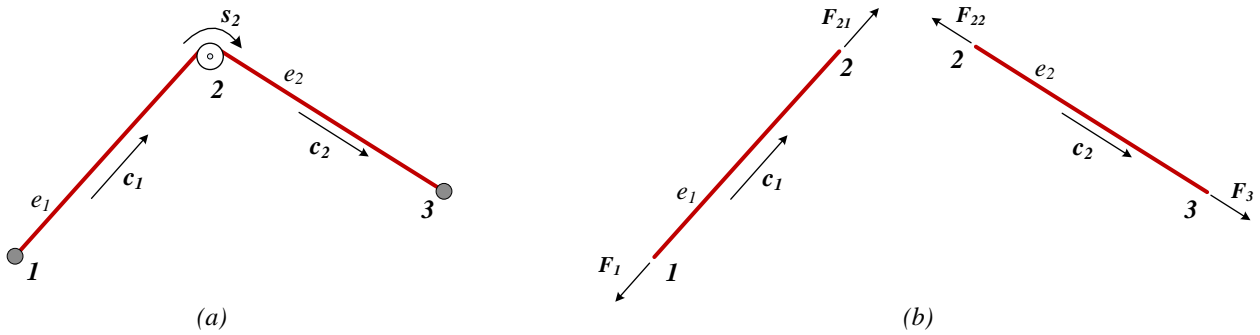


Figure 1. (a) A two element clustered cable, (b) Forces acting on cable nodes.

As mentioned earlier, ignoring friction effects at sliding nodes results in substantial model inaccuracy which cannot be neglected. For accurate modeling of sliding cable behavior, friction at sliding nodes must be taken into account

Consider the structure shown in Fig. 1(a). At node 2, suppose that friction exists at the contact area between the sliding cable and the pulley. Friction at this node resists relative motion between the two cable sub-elements. When resistance due to friction at this node is low, cable sliding is possible. When friction lock arises and the frictional resistance at contact area is great enough to hinder the cable from sliding, the internal forces at two sub-elements of the continuous cable can be expressed as:

$$\begin{aligned}
t_1 &= EA \frac{l_1 - \bar{l}_{0,1}}{\bar{l}_{0,1}} ; \quad \bar{l}_{0,1} = l_{0,1} - s_2 \\
t_2 &= EA \frac{l_2 - \bar{l}_{0,2}}{\bar{l}_{0,2}} ; \quad \bar{l}_{0,2} = l_{0,2} + s_2
\end{aligned} \tag{8}$$

In this situation, the sliding magnitude at node 2, s_2 , changes the non-loaded lengths of the two sub-elements ($\bar{l}_{0,1}$ and $\bar{l}_{0,2}$). In the absence of friction, modification of sub-element non-loaded lengths does not affect the distribution of axial forces since only the non-loaded length of the entire cable is considered. However, this is not the case for frictional sliding. To model static the behavior of a continuous cable, the sliding length needs to be included with the nodal displacements.

Equilibrium at nodes 1, 2 and 3 can be written in terms of the sub-element tension, t_1 and t_2 , in component form:

$$\begin{aligned}\mathbf{F}_1 &= -\mathbf{c}_1 t_1 \\ \mathbf{F}_2 &= \mathbf{c}_1 t_1 - \mathbf{c}_2 t_2 \\ \mathbf{F}_3 &= \mathbf{c}_2 t_2\end{aligned}\tag{9}$$

The system of equilibrium equations (Eq.9) is no longer sufficient for the analysis of the continuous cable while taking into account the frictional effects. Considering force equilibrium in three dimensions for the simple structure shown in Fig. 1, there are ten unknowns (the sliding length, s_2 , and the nine nodal displacements) but only nine equations. The additional equation is obtained through the relation between the tension forces around the sliding node.

Consider the two forces at pulley edges at node 2 in Fig. 2(a). These forces result from axial forces in the two cable sub-elements arriving at the pulley. Eq.10 expresses the relationship between forces at both sides of sliding node [13]:

$$t_2 = \alpha t_1\tag{10}$$

Eq.10 is known as capstan equation. It describes the relationship between the hold force and the pull force at the two ends of the sliding surface at the instant of impending slip [38]. The force ratio α in Eq.10 is given by:

$$\alpha = e^{\text{sign}(s_2)\mu\theta}\tag{11}$$

The force ratio is a function of the angle of contact, θ , defined in Fig. 2(b) and the coefficient of friction, μ , between the pulley and the cable. The ratio between the tension forces, t_1 and t_2 , depends also on the sliding direction i.e. $sign(s_2)$ in Fig 2 (a).

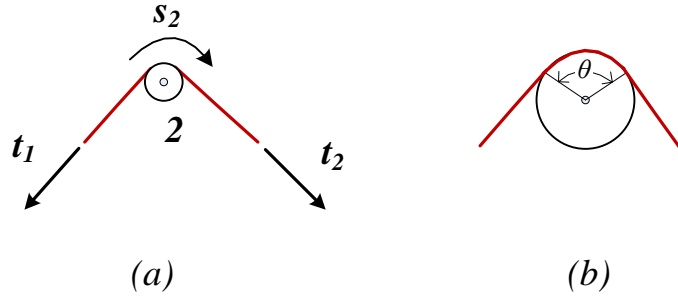


Figure 2. (a) cable-induced forces acting on a pulley; (b) contact angle.

Substituting Eq. 11 in t_1 and t_2 (Eq.8), an equivalent force relation at the sliding node (Eq.10) is written in terms of sliding length, s_2 , as follows:

$$\frac{l_2 - l_{0,2} - s_2}{l_{0,2} + s_2} = \alpha \frac{l_1 - l_{0,1} + s_2}{l_{0,1} - s_2} \quad (12)$$

Eq.12 is nonlinear in s_2 and for a defined geometric configuration (defined nodal coordinates and element lengths) it can be solved iteratively.

Additional equations similar to Eq.12 can be written for nodes 1 and node 3 if these nodes allow cable sliding. This is typically the case for a continuous cable sliding over multiple nodes. For example, consider the continuous cable of Fig. 3.

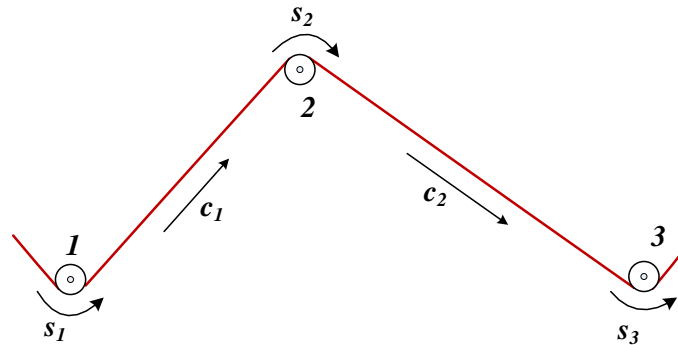


Figure 3. A clustered cable sliding over three pulleys.

When the clustered cable slides over the pulleys at nodes 1, 2 and 3 by sliding lengths, s_1 , s_2 and s_3 , internal forces at two sub-elements of the clustered cable are expressed as:

$$\begin{aligned} t_1 &= EA \frac{l_1 - \bar{l}_{0,1}}{\bar{l}_{0,1}} \quad ; \quad \bar{l}_{0,1} = l_{0,1} + (s_1 - s_2) \\ t_2 &= EA \frac{l_2 - \bar{l}_{0,2}}{\bar{l}_{0,2}} \quad ; \quad \bar{l}_{0,2} = l_{0,2} + (s_2 - s_3) \end{aligned} \quad (13)$$

Combining equations related to sliding nodes, the obtained system of nonlinear equations can be solved iteratively to yield values of sliding lengths s_1 , s_2 and s_3 . A new formulation of DR including sliding-lengths determination is described in the next section. This extends DR to accommodate friction effects in tensioned structures including continuous cables.

3. The proposed DR implementation

The static solution of both linear and non linear structures subject to load may be regarded as the limiting equilibrium state of damped structural vibrations. A static analysis case can be transformed into a pseudo-dynamic analysis case by introducing fictitious inertia and damping terms transforming a static equilibrium equation into an augmented equation of motion. The aim is to solve the augmented equation of motion using an explicit finite difference discretization. DR traces the motion of each node of an artificially damped structure until it comes to rest in a static equilibrium state. A key feature of the method is that mass and damping parameters do not need to be representative of the physical problem. Instead, damping, mass and time increments are chosen to obtain the fastest convergence to equilibrium. Theoretically, the convergence rate can be characterized in terms of the spectral radius of the iterative error equation [7]. Papadrakakis [39] carried out an error analysis and suggested an automatic procedure for the selection of DR parameters ensuring optimum convergence. The determination of optimal DR parameters has also been the subject of intensive research work [40-42].

Before presenting the new formulation of DR, an overview of the governing equations of this method is given to provide the necessary background.

3.1 Governing equations

The DR method follows from augmenting static equilibrium equations (Eq.14) by including inertial and damping terms (Eq.15):

$$\mathbf{f}_{int}(\mathbf{u}) = \mathbf{f}_{ext} \quad (14)$$

$$\{\mathbf{M} \dot{\mathbf{v}} + \mathbf{C} \mathbf{v}\} + \mathbf{f}_{int}(\mathbf{u}) = \mathbf{f}_{ext} \quad (15)$$

In Eq.14 and Eq.15, \mathbf{u} and \mathbf{v} are vectors of nodal displacements and velocities, \mathbf{M} and \mathbf{C} are mass and damping matrices, \mathbf{f}_{int} is the vector of internal forces and \mathbf{f}_{ext} is the vector of external forces. Introducing the residual force vector \mathbf{r} as the difference between external and internal forces at any time t , Eq.15 can be written as Eq.16.

$$\mathbf{M} \dot{\mathbf{v}}^t + \mathbf{C} \mathbf{v}^t = \mathbf{r}^t \quad (16)$$

Due to damping, nodal velocity and acceleration values decay to zero as the solution is approached. The transient response is attenuated leaving the steady state solution for the applied load. Static equilibrium is thus attained when the out-of-balance or residual forces converge to zero.

Using central differences, Eq.16 is discretized in time. Approximations for temporal derivatives are given by:

$$\mathbf{v}^t = \frac{1}{2}(\mathbf{v}^{t+\Delta t/2} + \mathbf{v}^{t-\Delta t/2}), \quad \dot{\mathbf{v}}^t = \frac{1}{\Delta t}(\mathbf{v}^{t+\Delta t/2} - \mathbf{v}^{t-\Delta t/2}) \quad (17)$$

Using these approximations, Eq.16 can be re-arranged to give the recurrence equations for nodal velocities:

$$\mathbf{v}^{t+\Delta t/2} = \left[\frac{1}{\Delta t} \mathbf{M} + \frac{1}{2} \mathbf{C} \right]^{-1} \left[\frac{1}{\Delta t} \mathbf{M} - \frac{1}{2} \mathbf{C} \right] \mathbf{v}^{t-\Delta t/2} + \left[\frac{1}{\Delta t} \mathbf{M} + \frac{1}{2} \mathbf{C} \right]^{-1} \mathbf{r}^t \quad (18)$$

The velocities are then used to predict displacements at time $(t + \Delta t)$:

$$\mathbf{u}^{t+\Delta t} = \mathbf{u}^t + \Delta t \mathbf{v}^{t+\Delta t/2} \quad (19)$$

The iterative process of DR method consists of a repetitive use of Eq.18 and Eq.19. The process continues until the residual forces converge to zero. In the classic formulation for DR, mass and damping parameters have to be chosen to ensure that the recurrence procedure converge to static equilibrium [7, 43, 44]. Generally, a diagonal mass matrix and a mass-proportional damping matrix are used. An efficient alternative is the use of kinetic damping [31, 39, 45]. When kinetic damping is employed, viscous damping coefficients in Eq.18 are no longer needed and the recurrence equation for nodal velocities reduces to Eq.20:

$$\mathbf{v}^{t+\Delta t/2} = \mathbf{v}^{t-\Delta t/2} + \Delta t \mathbf{M}^{-1} \mathbf{r}^t \quad (20)$$

As DR iterations proceeds, kinetic energy of the structure is calculated. When a kinetic energy peak is detected, all nodal velocities are set to zero and the current coordinates are taken as initial values for the next iteration. The analysis progressively eliminates the kinetic energy from various modes of vibration until of convergence. Kinetic damping eliminates the need to compute optimized viscous-damping coefficients and offers a substantial reduction in the number of iterations [46]. Furthermore, this strategy efficiently accommodates geometrical inaccuracies and stiffness modifications [28].

3.2 Fictitious mass calculation

The mass matrix is built to improve the kinetic damping while keeping numerical stability. It is commonly chosen as a stiffness-proportional diagonal matrix [47]. Based on these assumptions, Underwood [7] proposed the use of the circle theorem of Gerschgorin which permits to obtain upper bounds to the eigenvalues of the recurrence matrix ($\mathbf{M}^{-1} \mathbf{K}$). For a defined time step, this theorem gives the following general expression that must be satisfied for mass terms in order to guarantee the stability of the iterations.

$$M_i \geq \frac{1}{4} \Delta t^2 \sum_j |k_{i,j}| \quad (21)$$

In Eq.21, $k_{i,j}$ are the elements of the tangent stiffness matrix.

According to Barnes [31], the mass at any node i should be set to comply with Eq.22 in order to guarantee the stability of the iterations for an arbitrarily chosen value of the time increment Δt . The stiffness term, $k_{i,x}$, is calculated for each node i and for each direction x by the summation of contributions from all members meeting at the node.

$$M_{i,x} = \left(\frac{\Delta t}{0.5} \right)^2 \frac{k_{i,x}}{2} \quad (22)$$

The latter formulation proposed by Barnes [31] is used in this work. A thorough description of the DR algorithm is given in [32].

3.2 Residual forces

The modification introduced to DR is concerned with the calculation of the residual forces. Since sliding-induced friction directly affects the distribution of internal forces in continuous cables, residual forces are affected.

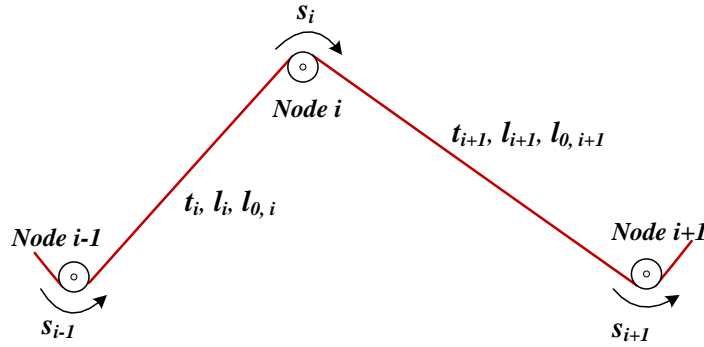


Figure 4. A generic clustered cable with multiple sliding nodes.

At each time step t , Eq.19 is used to determine current node coordinates. The updated member-length vector follows immediately and for each continuous cable, sub-element current lengths are determined. A system of nonlinear equations relating sliding lengths to current sub-element lengths is thus formulated. Each equation in the system explicitly represents the relation between axial forces at both sides of a sliding node. Consider the generic sliding node i in Fig. 4, the equation relating tension forces t_i and t_{i+1} is:

$$\frac{l_{i+1} - l_{0,i+1} - s_i + s_{i+1}}{l_{0,i+1} + s_i - s_{i+1}} = \exp(\text{sign}(s_i) \mu \theta) \frac{l_i - l_{0,i} - s_{i-1} + s_i}{l_{0,i} + s_{i-1} - s_i} \quad (23)$$

The force ratio, α_i , is calculated for each sliding node based on the updated geometry of the structure. A trust-region algorithm is employed to solve the obtained system of nonlinear equations [48]. Once sliding lengths are determined, the internal forces at all cable sub-elements are thus calculated based on Eq.13. This is repeated for all continuous cables. For all other members of the structure (struts and discontinuous cables) the internal forces are calculated based on the current geometry.

Once the vector of internal forces in the structure is determined, residual forces can be calculated. For any node i , the residual force in x -direction $r_{i,x}$ is the sum of the external force $f_{ext,i,x}$ and the x -component of the resultant force induced by the contributions of the N members meeting at node i .

$$R_{i,x}^t = f_{ext,i,x} + \sum_{m=1}^N \frac{t_m^t}{l_m^t} (x_{j,m}^t - x_{i,m}^t) \quad (24)$$

Eq.24 gives the expression of the x -component of the residual force at node i where t_m^t and l_m^t are tension and length of member m connecting node i to node j . Similar equations may be written for the y and z coordinate directions. The procedure for residual force calculation is listed in Table 1.

Table 1: Algorithm for residual force calculation

I. Inputs	At any time step, t : Updated nodal coordinates Element properties: Young modulus, E_m ; cross-section area, A_m and rest-length, $l_{0,m}$
II. For each continuous cable	(1) Calculation of element length for all members, l_m^t (2) For each sliding node i : - Calculate the ratio α_i based on current geometry - Establish i^{th} sliding equation based on Eq.21

(3) Iteratively solve the system of equations to obtain sliding lengths

(4) Calculation of sub-element internal forces based on Eq.13

III. For all other members (non continuous cables and bars)

(5) Calculation of internal forces

$$t_m^t = \frac{E_m A_m}{l_{0,m}} (l_m^t - l_{0,m})$$

IV. Test cable slackness and evaluate residual forces

(6) If (cable element and compression force): $t_m = 0$

(7) Calculation of residual force based on Eq.22

(8) Reset the residuals of all fixed or partially constrained nodes to zero

4. Numerical examples

In this section, three case studies are presented and discussed in order to show the efficiency of the DR extended-formulation in predicting the response of tensioned cable structures with sliding-induced friction. The efficiency of the new DR-formulation is first demonstrated through analysis of a continuous cable sliding through fixed nodes. This configuration is reported in the literature, thereby allowing a comparison of analysis results. In the second case study, load-response and actuation of a tensegrity beam are numerically simulated. The third case study is concerned with the deployment of a tensegrity-based footbridge where simulation results are compared with experimental findings.

4.1 A continuous cable sliding through fixed nodes

The performance of the friction-based DR formulation is demonstrated using an example of a continuous cable originally presented by Ju and Choo [16]. The example consists on static analysis of a continuous cable sliding through two nodes, as shown in Fig. 5. Ju and Choo [16] has employed a FE formulation for a cable passing over multiple pulleys taking into account friction effects.

The continuous cable system displayed in Fig. 5 is fixed at node 1 and slides at fixed node 2 and node 3. The cable is assumed linear elastic, weightless and undamped. It has a total length of 240 cm and a cross section area of 0.6 cm². It is made of stainless-steel with a Young modulus of 11500 kN/cm². The cable is divided into three sub-elements: L_1 , L_2 and L_3 having 100 cm, 40 cm and 100 cm length. A pulling force, $P=30$ kN, is applied at the end of the cable (node 4). A friction coefficient $\mu=0.1$ is considered and the contact angle, θ , is equal to $\pi/2$ at node 2 and $\pi/4$ at node 3.

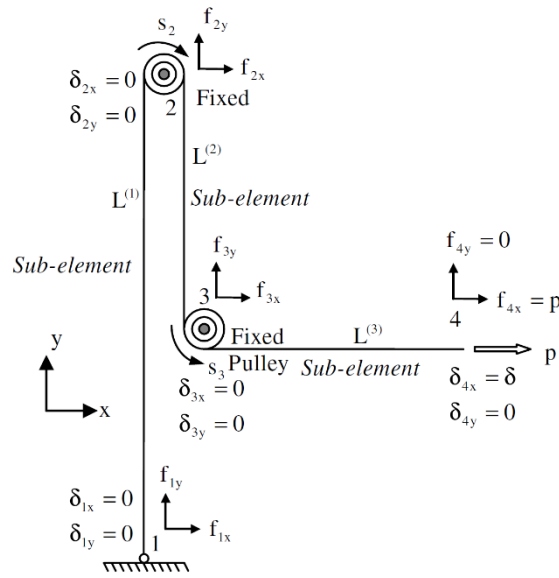


Figure 5. A continuous cable sliding through two fixed nodes (taken from Ju and Choo [16]).

The structure is studied using the new DR formulation. Internal force results are compared with those obtained by the application of the FE procedure proposed by Ju and Choo [16].

Table 2: Analysis results for the continuous cable case study

	DR	FE (Ju and Choo [16])
Tension in L_1 (kN)	23.7	23.7
Tension in L_2 (kN)	27.7	27.7
Tension in L_3 (kN)	30.0	30.0
Sliding magnitude s_1 (cm)	0.34	0.34
Sliding magnitude s_2 (cm)	0.50	0.50
Displacement δ at node 4 (cm)	0.93	0.93

Table 2 presents analysis results for the studied structure. Results for sub-element internal forces, sliding magnitudes and horizontal displacement at node 4 show agreement between the DR analysis and the FE-based results reported in the literature. The formulation proposed by Ju and Choo [16] is based on linear elastic assumptions and does not include geometric nonlinearities. However, this does not affect result comparison since the geometric nonlinearity does not affect the structure behavior in this peculiar example because sliding nodes are fixed.

4.2 A tensegrity-based beam

In this second case study, a tensegrity-based beam studied by Moored and Bart-Smith [18] is analysed employing the new DR formulation. The structure is composed of an assembly of three quadruplex modules. The detailed description of structure can be found in Bel Hadj Ali et al [32].

A perspective view of the tensegrity beam is given in Fig. 6 where thick lines denote bars and thin lines denote cables. Three of the end nodes of the structure (nodes 1, 3 and 6) are pinned forming a cantilever beam. Ten cable elements of the top surface and ten cable elements of the bottom surface of the structure are grouped into four continuous cables. In Fig. 7, continuous cables are shown in dashed lines in a top view of the tensegrity beam. Each continuous cable is attached to two end-nodes and slides through four intermediate nodes.

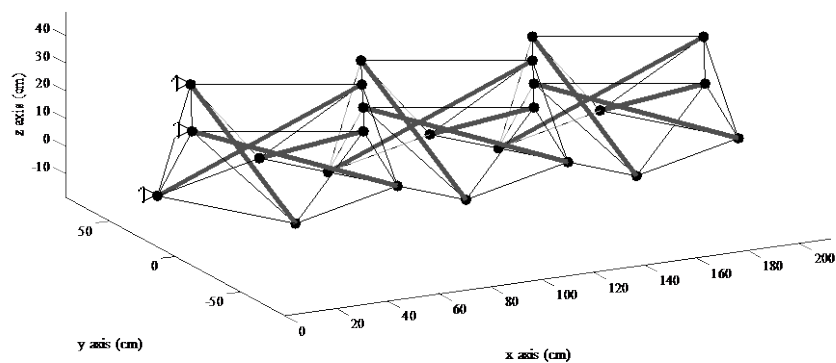


Figure 6. A perspective view of the tensegrity beam

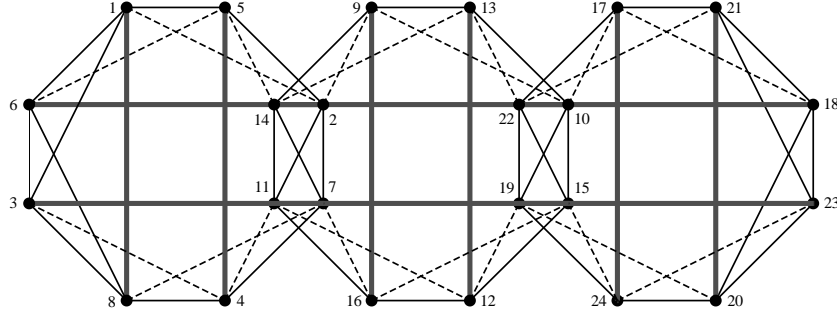


Figure 7. Top view of the tensegrity beam (dashed lines illustrate continuous cables)

The tensegrity beam used in this study has a length of 212 cm, a width of 80 cm and a height of 30 cm. Struts are made of aluminum hollow tubes with a length of 85 cm. All cable members are made of stainless-steel. Material and element characteristics are summarized in Table 3. Struts are modeled as flexible bars with elastic linear behavior. Cables are modeled as flexible strings with linear elastic behavior supporting only tension forces. In addition, it is assumed that actuation is performed through small and slow steps such that inertia effects can be neglected when the structure is in motion.

Table 3: Material characteristics for the tensegrity beam

Member	Material	Cross-section area (cm ²)	Young modulus (kN/cm ²)	Specific weight (kN/cm ³)
Struts	Aluminum	2.55	7000	$2.7 \cdot 10^{-5}$
Cables	Stainless-steel	0.5026	11500	$7.85 \cdot 10^{-5}$

Load-response of the tensegrity beam is investigated employing the new DR formulation. Prior to loading, top continuous cables are contracted by 2% in order to introduce self-stress in the structure and counteract deflection induced by self-weight. The tensegrity beam is subjected to a vertical loads applied at node 18 and node 23. A simulation is first performed assuming that continuous cables slide with no friction over intermediate nodes. The load-displacement curve obtained by the new DR formulation is compared with the results obtained using available methodologies for analysis of tensioned structures with sliding cables. Three methods are used for comparison: the FE-based formulation proposed by Moored and Bart-Smith [18], the co-

rotational-based method proposed by Zhang et al [19, 20] and the Modified DR proposed by Bel Hadj Ali et al [32]. The results predicted by the new DR formulation are identical to those generated by the three previously mentioned methods when friction is not included (Fig. 8). This comparison supports the correctness of the new DR formulation for the case of no friction.

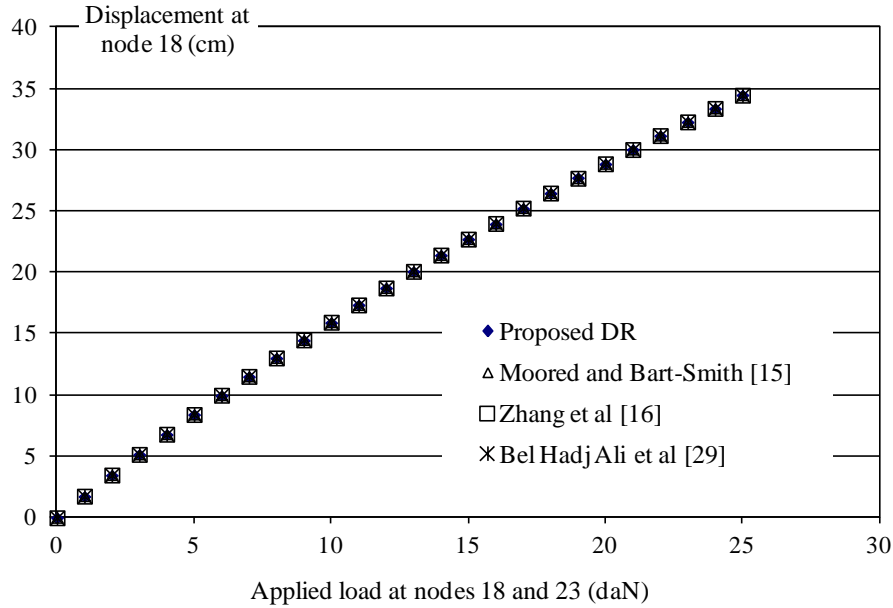


Figure 8. Load response of the tensegrity beam obtained using various analysis methodologies.

Load-response accounting for sliding-induced friction is also investigated. Various values for the coefficient of friction at contact surface between sliding cables and intermediate nodes are tested. Since the geometry of structure evolves minimally, the friction angle, θ , is kept constant and equal to $\pi/2$ for all sliding nodes. The structure is analyzed for varying values of the friction coefficient, μ , in order to investigate the influence of the friction on the structure behavior. Fig. 9 illustrates the evolution of internal axial force at cable 2 with respect to applied load at nodes 18 and 23. Cable 2 is a sub-element of the continuous cable connecting nodes 2 and 9 (Fig. 7). The applied forces are progressively increased from 5 to 30 daN. For the internal axial force at cable 2, the effect of friction is noticeable. Friction at sliding nodes causes an average tension decrease of 3.7% for a friction coefficient equal to 0.2. The internal force at cable 2 decreases by more than 11.5% for a friction coefficient equal to 0.4. The discrepancy between the values of axial forces with and without friction shows the importance of taking the frictional effect into

consideration. This is emphasized for tensioned cable structures that are highly sensitive to variation of axial forces at cable elements.

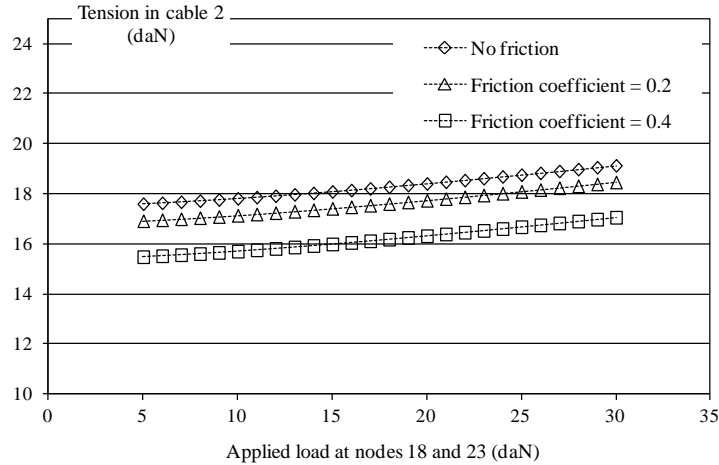


Figure 9. Evolution of the tension in cable 2 with respect to applied load for varying friction coefficient

Actuated bending deformation of the tensegrity beam is also studied. Bending deformation can be obtained through antagonist actuation of the of top and bottom continuous cables. Actuation is performed by changing the non-loaded length of active cables. For example, a prescribed actuation stroke of 20% is defined as a change in the non-loaded length of 20%. Prior to actuation, top continuous cables are contracted by 2% in order to introduce self-stress to counteract deflection induced by self-weight. The tensegrity beam is then actuated by changing the lengths of the four continuous cables. Top continuous cables are contracted by 10% while the bottom continuous cables are expanded by 10%. Contraction and elongation of active cables is made progressively by 1% length changes.

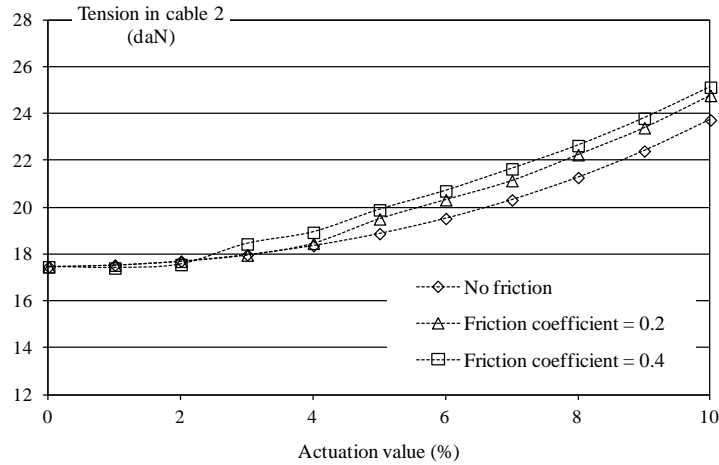


Figure 10. Evolution of the tension in cable 2 with respect to actuation value for varying friction coefficient

Fig. 10 illustrates the evolution of internal axial force at cable 2 with respect to the actuation percentage. At the end of the actuation sequence, sliding-induced friction with $\mu=0.2$ causes the internal force value at cable 2 to be more than 4% greater compared with tension values determined assuming no-friction. The axial force increases by more than 5% with $\mu=0.4$. The behavior during actuation of the tensegrity beam under consideration can be thought of as analogous to the tensioning process of prestressed cable structures such as cable domes. In such situations, even small deviations from design values could affect the behavior of the whole structure. This emphasizes the importance of accommodating the effects of friction when sliding cables are employed.

4.3 Deployment of a tensegrity footbridge

A four-module tensegrity footbridge is considered in this section. An elevation view of the tensegrity structure is given in Fig. 11(a). The structure is composed of four ring-shaped tensegrity modules. Symmetry about midspan is obtained by mirroring two modules. Basic modules are connected in a way that creates an empty space in their center for a walking space. The pentagon module contains 15 nodes describing 3 pentagonal layers (Fig. 11(b)). It comprises 15 struts held together in space by 30 cables forming a ring-shaped tensegrity unit. Struts can be categorized into diagonal and intermediate based on their position. Diagonal struts connect outer and inner pentagon nodes while intermediate struts connect middle pentagon nodes to outer and

inner pentagon nodes. Cables are separated into 10 layer cables and 20 x-cables. Layer cables connect nodes of the two outer pentagons while x-cables connect middle pentagon nodes to inner and outer pentagon nodes. The 10 x-cables that are coplanar with the diagonal struts are called coplanar x-cables. In Fig. 11 (a) and (b), thick lines denote bars while thin lines denote cables.

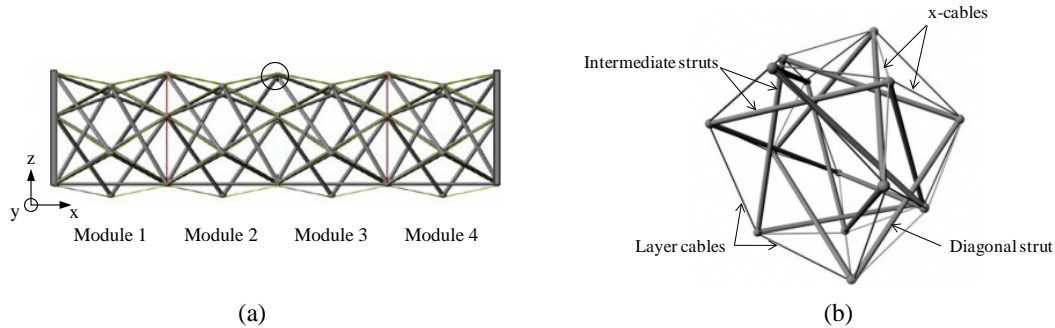


Figure 11. (a) an elevation view of the tensegrity structure and (b) a perspective view of the basic pentagon module.

A 4 m-span near-full-scale model of the footbridge was built to study deployment behavior [2, 3, 35, 36]. Fig. 12(a) illustrates a front view of one half of the tensegrity structure. Struts are made of structural steel (S355, 210GPa) hollow tube section profiles of 13.5 m length, a diameter of 28 mm and a thickness of 1.5 m. Cables have a diameter of 4mm and are made of stainless steel with a modulus of elasticity of 120 GPa. The layer cables are replaced by springs with a stiffness of 2 kN/m at the supports and 2.9 kN/m at other locations. Springs lengthen during folding, thereby assisting deployment as they shorten.

Each half of the structure is controlled by five continuous active cables. A two strut joint allowing continuous cable sliding is illustrated in Fig. 12(b). Each active continuous cable starts from a node connected to the support and ends at the front nodes. Top views of the footbridge in its folded and deployed configurations are given in Fig. 13. A detailed description of the structure could be found in Veuve et al [35, 36].

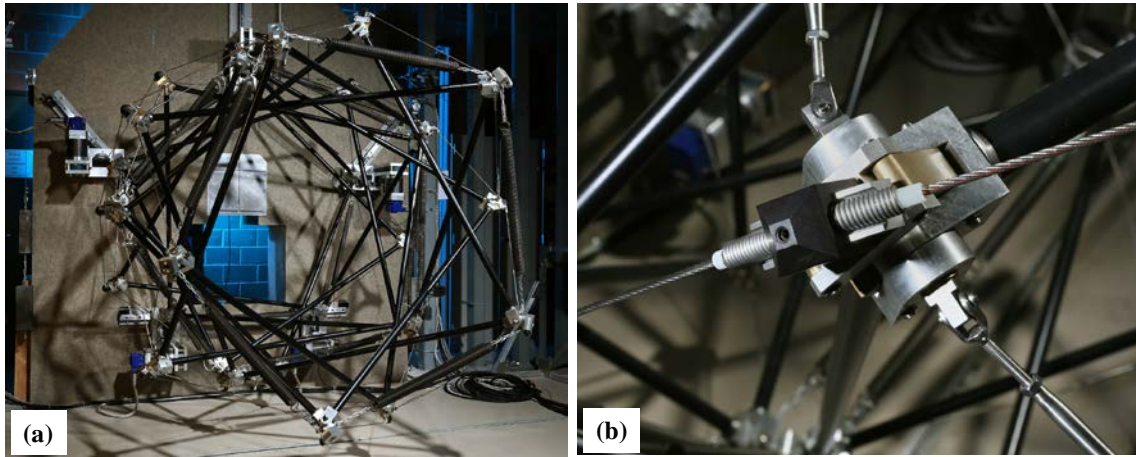


Figure 12. A front view of one half of the tensegrity structure (a) and a two strut joint allowing continuous cable sliding (b) (Credit IMAC/EPFL)

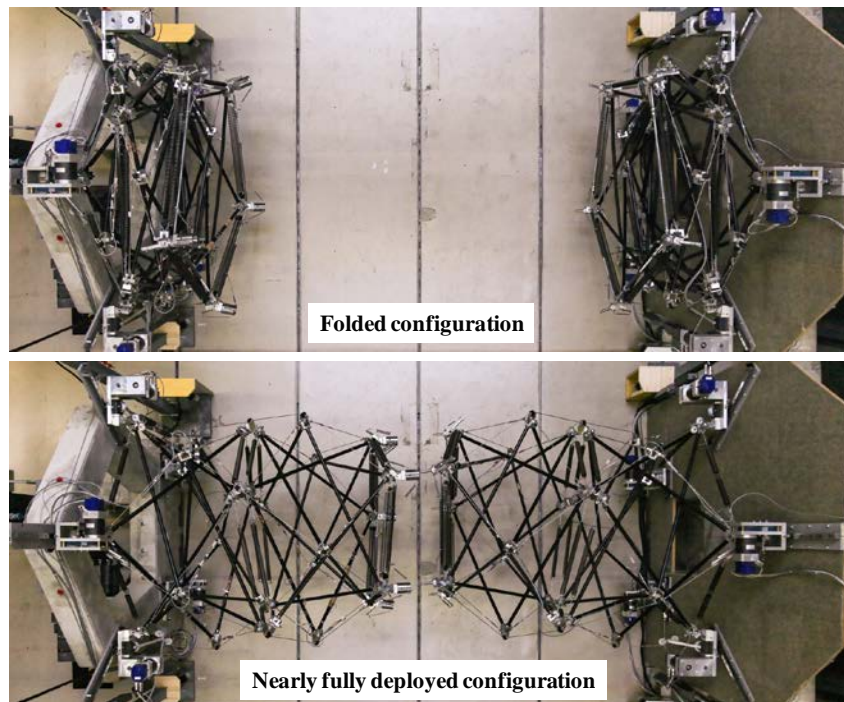


Figure 13. Top views of the tensegrity structure at folded configuration (top) and at nearly deployed configuration (bottom) (Credit IMAC/EPFL)

4.3.1 Deployment simulation

Deployment of the tensegrity footbridge was first studied by Rhode-Barbarigos et al [2, 3]. Veuve et al [35, 36] improved deployment strategy and performed mid-span connection of the footbridge. A purely geometrical study revealed that a contact-free deployment of the tensegrity system is feasible using cable control [3]. The deployment path was analyzed numerically using a modified DR algorithm assuming frictionless motions and quasi-static actuation [32]. Previous numerical studies of the deployment revealed that the deployment path can be composed of a series of intermediate equilibrium configurations. Moreover, deployment was found feasible with equal actuation-step size for all active cables. All previous deployment studies involved assumptions of friction-free sliding of the continuous active cables during folding and deployment of the bridge.

Struts are modeled as flexible bars with elastic linear behavior and all cables are modeled as flexible strings with linear elastic behavior supporting only tension forces. For deployment simulations, actuation is conducted in such way that the structure goes through successive equilibrium configurations. The simulated equilibrium configurations are close enough to create the deployment path. Moreover, a quasi-static deployment is assumed and dynamic effects are not taken into account in this study.

Sliding with friction is studied employing the new DR formulation. Deployment of one half of the footbridge is numerically simulated. Varying values of the friction coefficient, μ , are tested to evaluate the influence of the sliding-induced friction on the structure behavior. Deployment is simulated through application of equal actuation steps. Each actuation step is defined as a set of length changes of the active cables.

Fig. 14 and Fig. 15 illustrate the evolution of vertical and lateral displacements of the top node of the middle pentagon of the structure (node 20) with respect to the evolving structure length. The node under consideration is marked with a circle in Fig. 11(a). Three values of the friction coefficient are taken into account: 0, 0.1 and 0.2. Results displayed at Fig. 14 and Fig. 15 show that the node deviates from its friction-free trajectory during deployment. The discrepancy is

increasing with increasing value of the friction coefficient. Furthermore, a greater deviation is noticed in the first third of the deployment path. This indicates that the friction at sliding nodes is more pronounced at this deployment stage when the structure is close to its folded configuration. This is mainly related to the value of the contact angle at sliding nodes which progressively decreases during deployment in relation with the evolution of the shape.

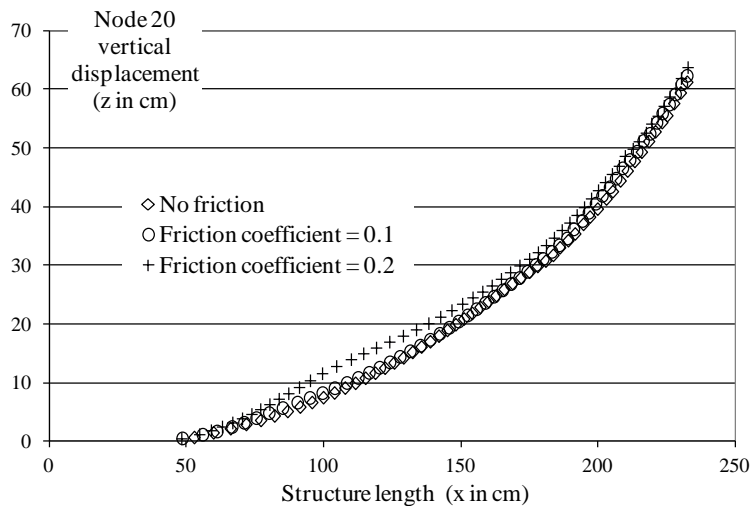


Figure 14. Vertical displacement of node 20 during deployment

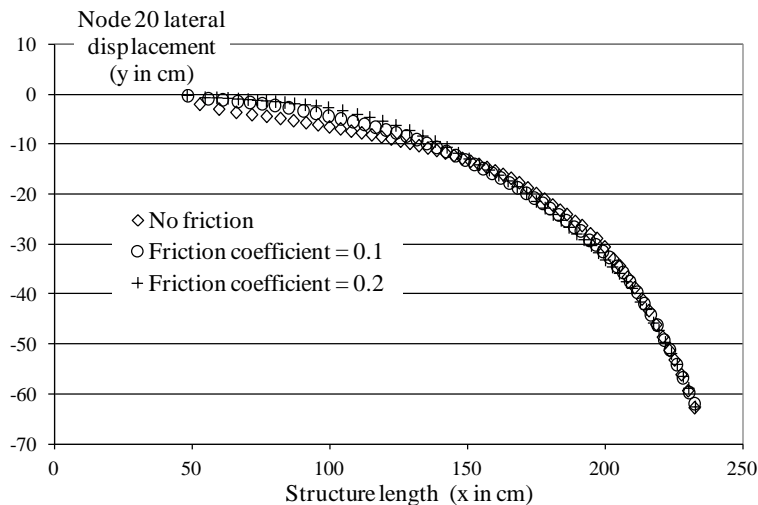


Figure 15. Lateral displacement of node 20 during deployment

The evolution of internal forces at two members is also studied. Fig. 16 illustrates the evolution of the tension in cable 85 with respect to the structure length during deployment. Cable 85 is a

sub-element of an active continuous cable which is connected to the middle pentagon of the footbridge. The friction-induced variation in axial forces is more pronounced than the deviation in nodal displacements. With a coefficient of friction equal to 0.2, the tension in cable 85 is nearly double of the friction-free value at some points of the deployment path. The same tendency is noticed for the compression value at strut 57. This element is an intermediate strut connected to the middle pentagon of the footbridge. Fig. 17 illustrates the evolution of the axial compression force in strut 57 with respect to the structure length during deployment. For the two elements under consideration, the differences between the axial forces with and without friction tend to decrease progressively during deployment.

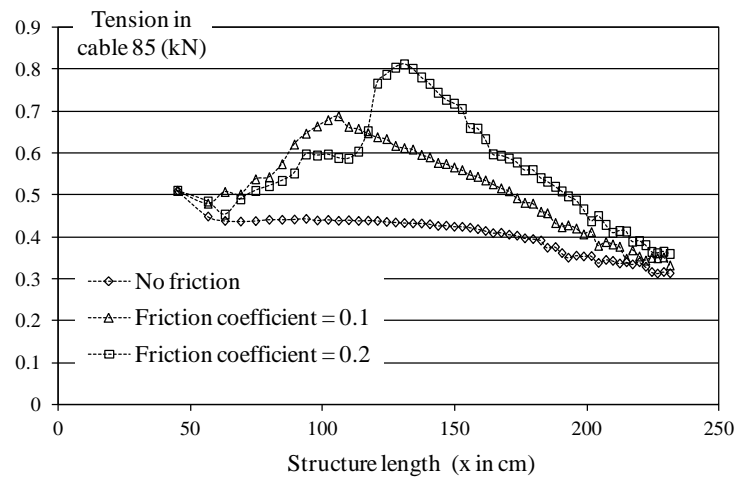


Figure 16. Tension in cable 85 during deployment

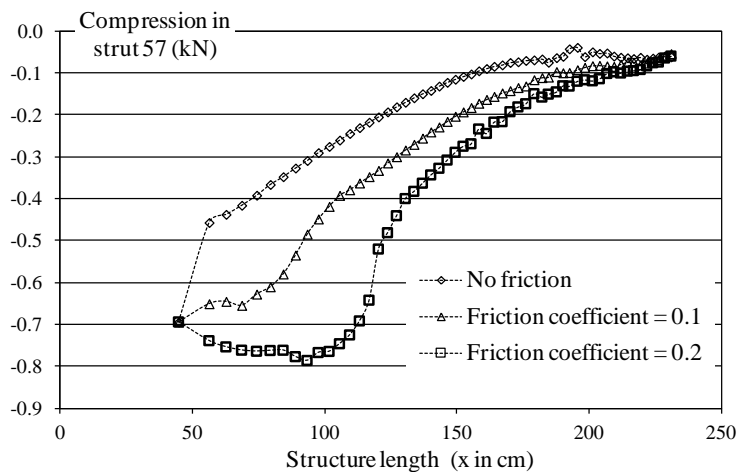


Figure 17. Compression in strut 57 during deployment

4.3.2 Experimental deployment

The deployment of the tensegrity structure with continuous actuated cables is studied on the near-full-scale physical model. Position measurements are performed with an optical tracking system. Some members are equipped with strain gauges in order to monitor axial forces during deployment. The structure is set at its fully folded length of 50 cm. Deployment tests show that when active cables are shortened equally and simultaneously, deployment is hindered by strut contact. Comparing experimental findings with model predictions reveals a substantial discrepancy with more than 20% deviation between predictions and measurements. This is mainly due to joint eccentricities and other complexities related to joint and support design.

In order to fully deploy the structure, Veuve et al [35] employed unequal length changes of active cables. Experimentally-determined deployment paths and corresponding actuation sequences have been proposed in order to minimize the effect of sliding-induced friction and joint eccentricities during deployment. The actuation sequence by Veuve et al [35] is employed here for the analysis of the deployment of the tensegrity structures. Recently, Sychterz and Smith [37] experimentally characterized the friction at the joints of the deployable structure. They showed that the friction coefficient ranges between 0.1 and 0.15. These values are taken into account in this study.

Fig. 18 illustrates the evolution of the vertical displacements of node 20 measured on the near-full-scale physical model with respect to the structure length during deployment. Experimental measurements are compared with simulated values obtained with the new DR formulation for friction coefficients equal to 0, 0.1 and 0.15. Results show discrepancy between measurements and predictions with frictionless sliding. This confirms previous results obtained by Veuve et al. [35]. However, the discrepancy between measurements and predictions decreases when friction is taken into account. For the first 2/3 of the deployment path, DR with a coefficient of friction equal to 0.15 predicts the vertical displacement of node 20 with less than 5% error. In the last third of the deployment path, DR predictions with friction coefficient equal to 0.1 are hardly distinguished from those obtained with friction coefficient equal to 0.15. At the end of the

deployment, displacement prediction of node 20 is slightly overestimated with respect to the measurement.

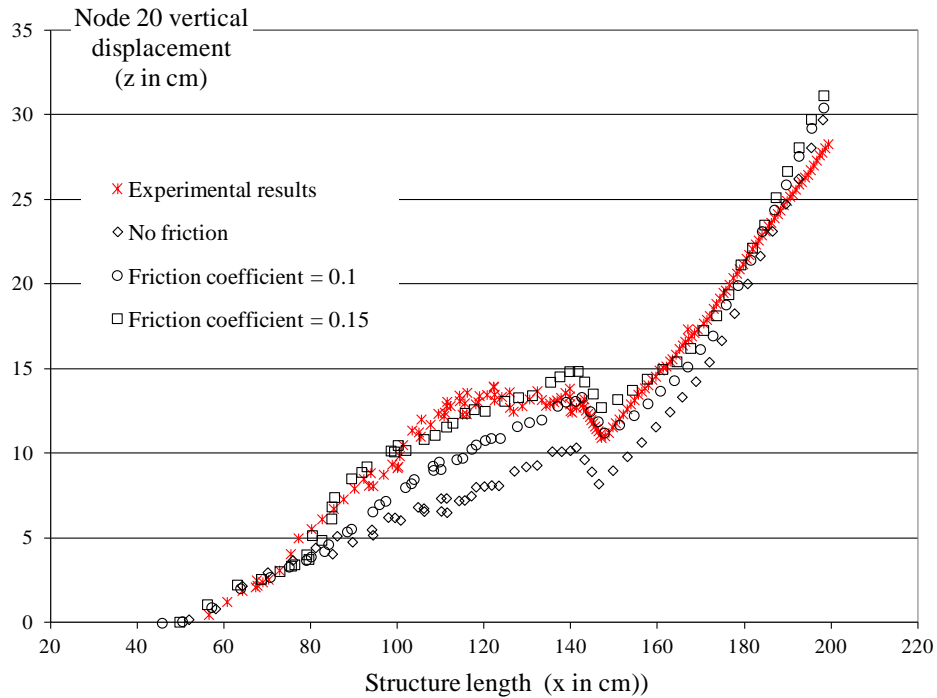


Figure 18. A front view of one half of the tensegrity structure

Axial force measurements are also compared with DR predictions. Two x-cables are studied: the first one is situated in the first module near to the supports of the structure and the second one is situated in the second module and connected to the middle pentagon nodes. Fig. 19 illustrates the evolution of the tension in cable 73 with respect to actuation steps during deployment. Cable 73 is an x-cable connected to the middle pentagon of the footbridge. Comparing experimental measurements to simulation results shows that including sliding-induced friction improves prediction accuracy. This is evident between actuation steps 20 and 60 and with a coefficient of friction equal to 0.1. In other parts of the deployment path, prediction improvement is not obvious.

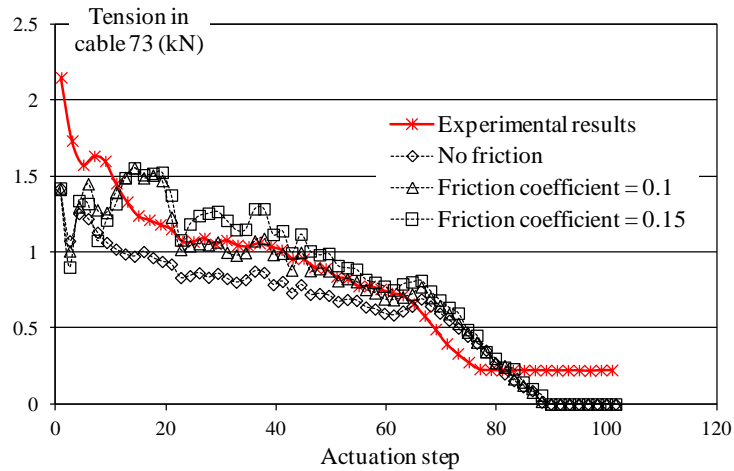


Figure 19. Tension in cable 85 during deployment

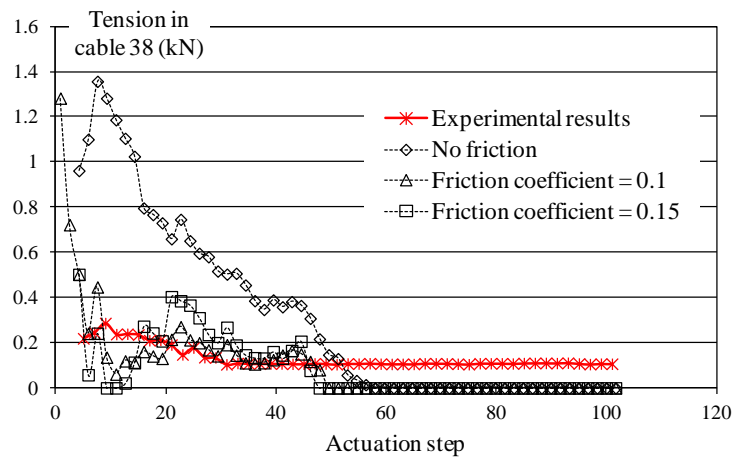


Figure 20. Compression in strut 57 during deployment

Fig. 20 illustrates the evolution of the tension in cable 38 with respect to actuation steps during deployment. Cable 38 is an x-cable which is connected to one support of the footbridge. Taking into account sliding-induced friction improves substantially the accuracy of the DR-based predictions. However, simulations predict the cable goes slack in the second half of the deployment path while it remains slightly tensioned in the physical model.

5. Conclusions

Dynamic relaxation is an attractive static analysis method for cable structures. The method is extended here to accommodate continuous cables with sliding-induced friction. The concept of cable clustering is a scalable solution that is employed in engineering applications such as domes, tensioned membranes and tensegrity structures. Continuous cables simplify the tensioning process of cable domes and tensioned membranes. In active structures, connecting cable-elements reduces the number of actuators needed for active control and deployment. However, sliding-induced friction affects the mechanics of structural systems leading to challenges for structural analysis, control and actuation.

This study shows that the DR correctly accommodates continuous cables with sliding-induced friction. The first case study showed that the results obtained using the method proposed in this paper are in good accordance with existing FE-based methods. In contrast with the FE formulation of Ju and Choo [16], the new DR formulation accommodates geometric nonlinearities, which is a key advantage for the analysis of tensioned cable structures. The correctness of the proposed method is also demonstrated through analysis of a tensegrity-based beam in the second case study.

The numerical and experimental investigations presented for the deployment study of a near-full-scale tensegrity footbridge reveal some limitations. Sliding-induced friction improves DR predictions when compared with experimental findings. However, such improvements do not lead to perfectly accurate analyses. The method is clearly unable to overcome difficulties related to the behavior of the physical model such as eccentricities and complex joint behavior. Moreover, the discrepancy between experimental results and DR predictions may be due to the dynamic effects that are ignored in quasi-static deployment simulations.

Finally, the new DR formulation could be seen as good progress toward satisfactorily modeling cable structure with sliding-induced friction. The DR formulation described in this paper has potential to be the starting point for further improvements involving more accurate models of joints and taking dynamics into account during deployment.

Acknowledgements

The authors would like to thank the Swiss National Science Foundation for supporting this work (FN Grant N° 200020-169026). The authors wish to express thanks to Dr. Gennaro Senatore for fruitful discussions. This work has been achieved during the stay of Professor Nizar Bel Hadj Ali at IMAC-EPFL as an Invited Professor funded by EPFL.

References

1. Sultan, C. and Skelton, R., *Deployment of tensegrity structures*. International Journal of Solids and Structures, 2003. **40**(18): p. 4637-4657.
2. Rhode-Barbarigos, L., Bel Hadj Ali, N., Motro, R., and Smith, I.F.C., *Design Aspects of a Deployable Tensegrity-Hollow-rope Footbridge*. International Journal of Space Structures, 2012. **27**(2-3): p. 81-95.
3. Rhode-Barbarigos, L., Schulin, C., Bel Hadj Ali, N., Motro, R., and Smith, I.F.C., *Mechanism-Based Approach for the Deployment of a Tensegrity-Ring Module*. Journal of Structural Engineering, 2012. **138**(4): p. 539-548.
4. Gantes, C.J., Connor, J.J., Logcher, R.D., and Rosenfeld, Y., *Structural analysis and design of deployable structures*. Computers & Structures, 1989. **32**(3-4): p. 661-669.
5. Yang, S. and Sultan, C., *Modeling of tensegrity-membrane systems*. International Journal of Solids and Structures, 2016. **82**: p. 125-143.
6. Aufaure, M., *A finite element of cable passing through a pulley*. Computers & Structures, 1993. **46**(5): p. 807-812.
7. Underwood, P., *Dynamic Relaxation*, in *Computational methods for transient analysis* 1983, Elsevier: Amsterdam p. 245-256.
8. Pauletti, R.M.O., Guirardi, D.M., and Gouveia, S. *Modelling sliding cables and geodesic lines through dynamic relaxation*. in *IASS Symposium 2009, Evolution and trends in Design, Analysis and Construction of Shell and Spatial Structures*. 2009. Valencia.
9. Hincz, K., *Nonlinear Analysis of Cable Net Structures Suspended From Arches with Block and Tackle Suspension System, Taking into Account the Friction of the Pulleys*. International Journal of Space Structures, 2009. **24**(3): p. 143-152.
10. Pargana, J.B., Lloyd-Smith, D., and Izzuddin, B.A., *Fully integrated design and analysis of Tensioned Fabric Structures: Finite elements and case studies*. Engineering Structures, 2010. **32**(4): p. 1054-1068.
11. Pauletti, R.M. and Pimenta, P.M., *Formulação de um elemento finito de cabo incorporando o efeito do atrito (Elemento de cabos escorregando)*. Revista internacional de métodos numéricos, 1995. **11**(4): p. 565-576.
12. Kwan, A.S.K. and Pellegrino, S., *Matrix formulation of macro-elements for deployable structures*. Computers & Structures, 1994. **50**(2): p. 237-254.
13. Zhou, B., Accorsi, M.L., and Leonard, J.W., *Finite element formulation for modeling sliding cable elements*. Computers & Structures, 2004. **82**(2-3): p. 271-280.
14. Chen, Z.H., Wu, Y.J., Yin, Y., and Shan, C., *Formulation and application of multi-node sliding cable element for the analysis of Suspen-Dome structures*. Finite Elements in Analysis and Design, 2010. **46**(9): p. 743-750.
15. Lee, K.H., Choo, Y.S., and Ju, F., *Finite element modelling of frictional slip in heavy lift sling systems*. Computers & Structures, 2003. **81**(30-31): p. 2673-2690.
16. Ju, F. and Choo, Y.S., *Super element approach to cable passing through multiple pulleys*. International Journal of Solids and Structures, 2005. **42**(11-12): p. 3533-3547.
17. Genovese, D., *Strutture tensegrity - Metodi di Analisi e Ricerca di Forma*, in *Dipartimento di Architettura, costruzioni, strutture* 2008, Universita` Politecnica delle Marche: Italy. p. 82.
18. Moored, K.W. and Bart-Smith, H., *Investigation of clustered actuation in tensegrity structures*. International Journal of Solids and Structures, 2009. **46**(17): p. 3272-3281.

19. Zhang, L., Gao, Q., Liu, Y., and Zhang, H., *An efficient finite element formulation for nonlinear analysis of clustered tensegrity*. Engineering Computations, 2016. **33**(1): p. 252-273.
20. Zhang, L., Lu, M.K., Zhang, H.W., and Yan, B., *Geometrically nonlinear elasto-plastic analysis of clustered tensegrity based on the co-rotational approach*. International Journal of Mechanical Sciences, 2015. **93**: p. 154-165.
21. Otter, J.R.H., *Computations for prestressed concrete reactor pressure vessels using dynamic relaxation*. Nuclear Structural Engineering, 1965. **1**(1): p. 61-75.
22. Day, A.S., *An introduction to dynamic relaxation*. The Engineer, 1965. **219**: p. 218-221.
23. Douthe, C. and Baverel, O., *Design of nexorades or reciprocal frame systems with the dynamic relaxation method*. Computers & Structures, 2009. **87**(21-22): p. 1296-1307.
24. Dang, H.K. and Meguid, M.A., *Evaluating the performance of an explicit dynamic relaxation technique in analyzing non-linear geotechnical engineering problems*. Computers and Geotechnics, 2009. **37**(1-2): p. 125-131.
25. Pan, L., Metzger, D.R., and Niewczas, M., *The Meshless Dynamic Relaxation Techniques for Simulating Atomic Structures of Materials*. ASME Conference Proceedings, 2002. **2002**(46520): p. 15-26.
26. Salehi, M. and Aghaei, H., *Dynamic relaxation large deflection analysis of non-axisymmetric circular viscoelastic plates*. Computers & Structures, 2005. **83**(23-24): p. 1878-1890.
27. Zhang, L., Maurin, B., and Motro, R., *Form-Finding of Nonregular Tensegrity Systems*. Journal of Structural Engineering, 2006. **132**(9): p. 1435-1440.
28. Wakefield, D.S., *Engineering analysis of tension structures: theory and practice*. Engineering Structures, 1999. **21**(8): p. 680-690.
29. Domer, B., Fest, E., Lalit, V., and Smith, I.F.C., *Combining Dynamic Relaxation Method with Artificial Neural Networks to Enhance Simulation of Tensegrity Structures*. Journal of Structural Engineering, 2003. **129**(5): p. 672-681.
30. Barnes, M., *Form and stress engineering of tension structures*. Structural Engineering Review, 1994. **6**(3-4): p. 175-202.
31. Barnes, M.R., *Form Finding and Analysis of Tension Structures by Dynamic Relaxation*. International Journal of Space Structures, 1999. **14**: p. 89-104.
32. Bel Hadj Ali, N., Rhode-Barbarigos, L., and Smith, I.F.C., *Analysis of clustered tensegrity structures using a modified dynamic relaxation algorithm*. International Journal of Solids and Structures, 2011. **48**(5): p. 637-647.
33. Pauletti, R.M.O. and Martins, C.B. *Modelling the slippage between membrane and border cables*. in *IASS Symposium 2009, Evolution and trends in Design, Analysis and Construction of Shell and Spatial Structures*. 2009. Valencia.
34. Liu, H., et al., *Precision control method for pre-stressing construction of suspen-dome structures*. Advanced Steel Construction, 2014. **10**(4): p. 404-425.
35. Veuve, N., Safaei, S.D., and Smith, I.F.C., *Deployment of a Tensegrity Footbridge*. Journal of Structural Engineering, 2015. **141**(11): p. 04015021.
36. Veuve, N., Dalil Safaei, S., and Smith, I.F.C., *Active control for mid-span connection of a deployable tensegrity footbridge*. Engineering Structures, 2016. **112**: p. 245-255.
37. Sychterz, A.C. and Smith, I.F.C., *Joint friction during deployment of a near-full-scale tensegrity footbridge*. Journal of Structural Engineering, in press, 2017.
38. Lubarda, V.A., *Determination of the belt force before the gross slip*. Mechanism and Machine Theory, 2015. **83**: p. 31-37.

39. Papadrakakis, M., *A method for the automatic evaluation of the dynamic relaxation parameters*. Computer Methods in Applied Mechanics and Engineering, 1981. **25**(1): p. 35-48.
40. Kadhodayan, M., Alamatian, J., and Turvey, G.J., *A new fictitious time for the dynamic relaxation (DXDR) method*. International Journal for Numerical Methods in Engineering, 2008. **74**(6): p. 996-1018.
41. Rezaiee-pajand, M. and Alamatian, J., *The dynamic relaxation method using new formulation for fictitious mass and damping*. Structural Engineering and Mechanics, 2010. **34**(1): p. 109-133.
42. Metzger, D.R., *Adaptive damping for dynamic relaxation problems with non-monotonic spectral response*. International Journal for Numerical Methods in Engineering, 2003. **56**(1): p. 57-80.
43. Brew, J.S. and Brotton, D.M., *Non-linear structural analysis by dynamic relaxation*. International Journal for Numerical Methods in Engineering, 1971. **3**(4): p. 463-483.
44. Senatore, G. and Piker, D., *Interactive real-time physics: An intuitive approach to form-finding and structural analysis for design and education*. Computer-Aided Design, 2015. **61**: p. 32-41.
45. Topping, B.H.V. and Khan, A.I., *Parallel computation schemes for dynamic relaxation*. Engineering Computations, 1994. **11**(6): p. 513-548.
46. Veenendaal, D. and Block, P., *An overview and comparison of structural form finding methods for general networks*. International Journal of Solids and Structures, 2012. **49**(26): p. 3741-3753.
47. Rodriguez, J., Rio, G., Cadou, J.M., and Troufflard, J., *Numerical study of dynamic relaxation with kinetic damping applied to inflatable fabric structures with extensions for 3D solid element and non-linear behavior*. Thin-Walled Structures, 2011. **49**(11): p. 1468-1474.
48. Conn, A.R., Gould, N.I.M., and Toint, P.L., *Trust Region Methods* 2000: Society for Industrial and Applied Mathematics.

This work is licensed under a Creative Commons Attribution-NonCommercial-NoDerivatives 4.0 International License

